Taylor & Francis
Taylor & Francis Group

Combustion Science and Technology

ISSN: 0010-2202 (Print) 1563-521X (Online) Journal homepage: http://www.tandfonline.com/loi/gcst20

Experimental and Numerical Investigation on Spark Ignition of Linearly Arranged Non-Premixed Swirling Burners

Edouard Machover & Epaminondas Mastorakos

To cite this article: Edouard Machover & Epaminondas Mastorakos (2017) Experimental and Numerical Investigation on Spark Ignition of Linearly Arranged Non-Premixed Swirling Burners, Combustion Science and Technology, 189:8, 1326-1353, DOI: 10.1080/00102202.2017.1294589

To link to this article: http://dx.doi.org/10.1080/00102202.2017.1294589

Accepted author version posted online: 21 Feb 2017.
Published online: 21 Feb 2017.

COMBUSTION SCIENCE AND TECHNOLOGY
2017, VOL. 189, NO. 8, 1326–1353
http://dx.doi.org/10.1080/00102202.2017.1294589

Taylor & Francis
Taylor & Francis Group

Experimental and Numerical Investigation on Spark Ignition of Linearly Arranged Non-Premixed Swirling Burners

Edouard Machover and Epaminondas Mastorakos

Department of Engineering, University of Cambridge, Cambridge, UK

ABSTRACT

The ignition characteristics of a non-premixed multiple-burner linear combustion chamber was investigated experimentally and numerically, focusing on the determination of the mechanisms driving flame propagation from burner to burner. For different inter-burner spacings, overall equivalence ratios and bulk velocities, measurements of the velocity field and the mixture fraction distribution have been performed, respectively, with laser doppler anemometry and planar laser-induced fluorescence of acetone in the un-ignited flow. It was shown that in every individual burner, gas mixes with air within a central recirculation zone (CRZ) where the mixture is flammable except in the axial central rich gas jet and the annular air jet. Flammable mixture from the CRZ is extracted by the annular jet and this results in the existence of bridges of positive flammability factor in the inter-burner region. These bridges allow flame fragments to travel from the CRZ of the ignited burner to the CRZ of the adjacent unignited one, leading to burner-to-burner flame propagation. The ignition probability that sparking within a burner results in ignition of the adjacent one was obtained by performing many separate ignition trials with a laser spark. Ignition probability contours were also computed using a previously developed stochastic low-order ignition model and a large eddy simulation (LES) time-averaged solution of the cold flow. The quantification of the probability a flame kernel leads to burner ignition explained the differences existing between experimental results and the model. The results presented in this article extend our understanding of the mechanisms underlying the global ignition behavior of non-premixed annular combustion chambers.

ARTICLE HISTORY
Received 13 October 2016
Revised 10 January 2017
Accepted 9 February 2017

KEYWORDS
Flame propagation; Gas turbines; Ignition probability; Light-round; Non-premixed flames; Spark ignition

Introduction

In the context of high altitude engine relight, the trend towards lean operation addresses a new challenge brought by the need to ignite successfully the combustion chamber (Lefebvre, 1999; Mastorakos, 2009). Currently, the complexity and the lack of knowledge of the physics of the phenomena limit the ability to predict, at the design stage, the ignitability of a gas turbine combustor leading to a large degree of technical compromise. Hence, more research is needed in order to assist with the design of new generation gas turbine combustors.

In the context of spark ignition in turbulent non-premixed mixtures, the stochasticity involved in the success of a spark event, given energy deposition, time, and location, can

CONTACT Edouard Machover edouard.machover@gmail.com Department of Engineering, University of Cambridge, Trumpington Street, Cambridge CB2 1PZ, UK.

Color versions of one or more of the figures in the article can be found online at www.tandfonline.com/gcst.

be analyzed through three distinct probabilities. The probability of finding flammable mixture at the spark location, the flammability factor, is defined as $F = \int_{\xi_{lean}}^{\xi_{rich}} P(\eta)\,\mathrm{d}\eta$, where ξ_{lean} and ξ_{rich} denote, respectively, the lean and rich flammability limits and P the probability density function (PDF) of the mixture fraction (Birch et al., 1981; see Mastorakos, 2009 for more details of this concept). P_{ker} is the probability of generating a kernel and P_{ign} is the probability of whole flame ignition.

In the context of single combustors, spark ignition has been well studied for non-premixed flames in various geometries, experimentally (Ahmed et al., 2007a; 2007b; Ahmed and Mastorakos, 2006, 2010, 2016), and numerically through large eddy simulation (LES) (Bulat et al., 2013; Jones et al., 2012; Jones and Prasad, 2011; Lacaze et al., 2009; Subramanian et al., 2010; Triantafyllidis et al., 2009). It was shown that ignition was sometimes possible when sparking outside the rich and lean flammability limits. This was attributed to strong convection of heat or radicals created at the spark of finite size towards the region of flammable mixture.

Furthermore, low-order ignition models have been developed in order to provide easier prediction of the ignition behavior in non-premixed and spray single burners (Eyssartier et al., 2013; Neophytou et al., 2012). The ignition behavior of a single bluff-body premixed burner was investigated with the low-order model provided by Neophytou et al. (2012) and Sitte et al. (2016), and it was shown that even for premixed flames where ignition has significant impact on the flow field, the model was able to predict accurately the effects of turbulent velocity fluctuations on the turbulent burning velocity as well as ignition probability contours. Recently, new functions have been implemented in the low-order model developed by Neophytou et al. (2012) and Soworka et al. (2013). The modified code showed its ability to predict with reasonable accuracy the most promising location for successful ignition in several combustor geometries. Recently, LES of laser ignition sequences were performed in order to predict ignition probability and to determine the mechanisms responsible for ignition success or failure (Escalpez et al., 2015). Ignition probability was obtained at three ignition locations in a swirled turbulent partially premixed single burner studied experimentally by Cordier et al. (2013). No correlation between local turbulent kinetic energy and ignition probability was observed, and it was shown that the early flame kernel development was critical for the success of ignition. Consequently, local flow properties together with an analysis of the trajectory of the kernel were required for predicting ignition probabilities. The simulations of Escalpez et al. (2015) were in good agreement with the experiments of Cordier et al. (2013) demonstrating the capability of the LES to capture the stochastic nature of ignition. Simulations showed that ignition success was characterized by flame kernel growth to a minimum size and its penetration in the recirculation zone of the burner, whereas ignition failure was associated with local mixture fraction out of the flammability limits and high turbulence level at spark location.

In realistic gas turbines, the practical problem of light-round (i.e., flame propagation from one burner to the adjacent one) implies additional physics; the mechanisms by which flame can propagate across a droplet-laden air flow, or an inhomogeneous fuel/air mixture, are problems that have not been studied enough. Light-round has been first investigated numerically for a helicopter engine with large-scale parallel computation

using LES (Boileau et al., 2008). It has been found that the gas expansion following successful ignition of a single burner was a mechanism involved in the flame expansion in the annular direction. The mean flow was considered responsible for the burner-to-burner propagation and the speed of light-round was found to be much greater than the turbulent flame consumption speed. It was suggested that this expansion helped the spreading of the flame from one combustor to the next one.

More recently, in premixed mode, an annular geometry consisting of a number of identical swirling premixed burners confined in a transparent enclosure has been studied by Bourgouin et al. (2013). The experimental results showed that the mechanisms responsible for flame displacement velocity were the normal burning velocity and the flow motion caused by the volumetric expansion across the flame. Additionally, the burned gases formed by buoyancy forces and ignited injectors were considered responsible for the convection of the flame downstream. These results were supported by numerical simulations based on a G-equation and by LES (Philip et al., 2014, 2015a, 2015b).

Effect of the inter-burner spacing on the burner-to-burner flame propagation was studied experimentally and numerically with LES for a linear configuration comprising five injectors where turbulent premixed combustion regime was considered dominant in the whole combustion chamber except in the vicinity of the burners (Barré et al., 2014). The authors have found that spacing between burners had an impact on the flame pattern as the ignition process varied from one injector to the subsequent one with a balance between two distinct modes. These are streamwise convection by the mean flow and spanwise propagation between burners. Streamwise convection, related to large spacing between burners, was associated to high variability and small burner-to-burner flame propagation speed, whereas spanwise propagation, dominant with lower inter-burner spacings, was associated to lower variability and greater lightround speeds. Fast capture of the flame by the adjacent burner during flame propagation was identified as the mechanism responsible for the latter propagation mode.

In non-premixed mode, Machover and Mastorakos (2015) investigated burner-to-burner propagation in an annular combustion chamber consisting of a number of non-premixed swirl burners equipped with a central bluff-body with axial fuel injection The global light-round behavior of the combustor was studied by investigating changes in spacing between burners (S), overall equivalence ratio (ϕ), and the bulk velocity (U_b). It was shown experimentally that, in the inter-burner region, flame kernel propagation was driven by favorable local conditions rather than by volumetric expansion, as evidenced in premixed configuration by Bourgouin et al. (2013) and Machover and Mastorakos (2017). Burner-to-burner propagation was based on events in which a flame fragment coming from the ignited burner penetrated fully in the recirculation zone of the adjacent un-ignited burner, usually from the downstream part of the recirculation zone, but that this was not always successful, giving rise to delays in the burner-to-burner propagation. Consequently, the time elapsed between two consecutive adjacent burner ignitions varied significantly during the full ignition sequence, suggesting a stochastic global behavior. The variability was found to increase with increasing S, increasing U_b, and decreasing ϕ. Furthermore, the overall speed of light-round increased with increasing number of burners and overall equivalence ratio, but remained rather constant when increasing bulk velocity.

Based upon these previous findings on annular non-premixed combustors, the aim of the present research is to explain through experiments and modeling the exact mechanism by which

the flame moves from one burner to the next one during the burner-to-burner propagation in non-premixed mode. First, the experimental configuration is described followed by the numerical setup. Then, the flow field is characterized by performing velocity and mixture fraction distribution measurements. Probability of ignition is then obtained experimentally and numerically. Finally, differences between experiments and simulations are discussed. The article concludes on the global mechanism driving burner-to-burner flame propagation.

Methods

Experimental methods

Apparatus

The burner used in the experiments of the present work is shown by a sketch in Figure 1 and a photo in Figure 2. It consists of five equally spaced bluff-body stabilized turbulent swirl non-premixed flames placed in a linear configuration. The apparatus is a linear adaptation of a non-premixed annular burner developed at the University of Cambridge (Machover and Mastorakos, 2015).

The air is exhausted through a flow divider connected to five identical 150-mm-long circular tubes with an inner diameter of $D = 18.9$ mm. Five burners were chosen for the sake of symmetry and avoidance of edge effects. Each tube is fitted with a centrally located duct that consists of a 5 mm diameter tube of 1.0 mm wall thickness. The value of 3 mm was chosen for the internal diameter in order to get close values of air and methane bulk

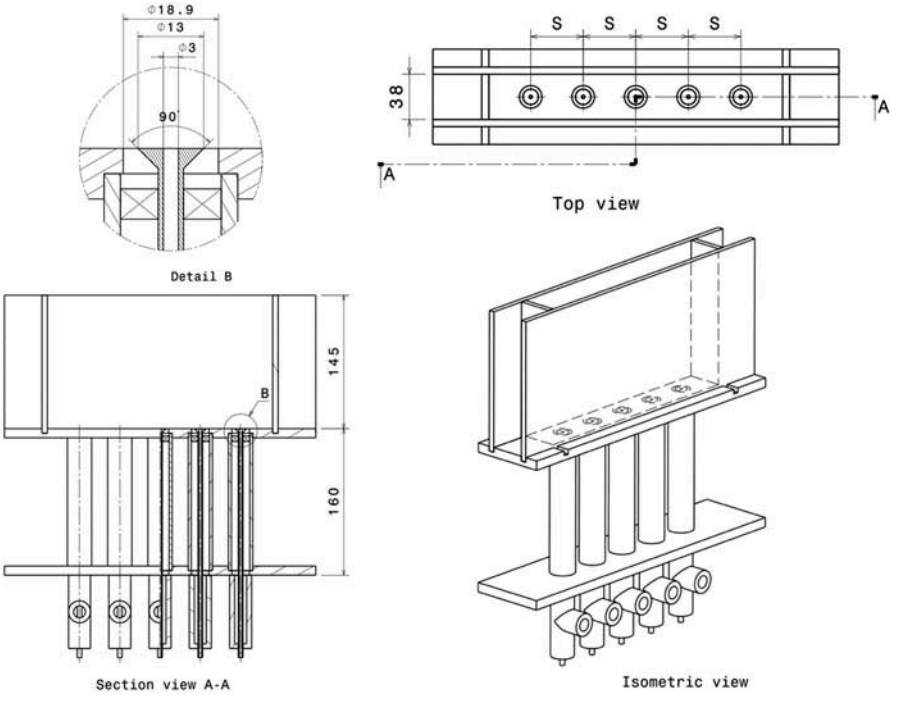

Figure 1. Drawing of the linear non-premixed combustor for an inter-burner spacing $S = S_{12}$. The dimensions are in mm.

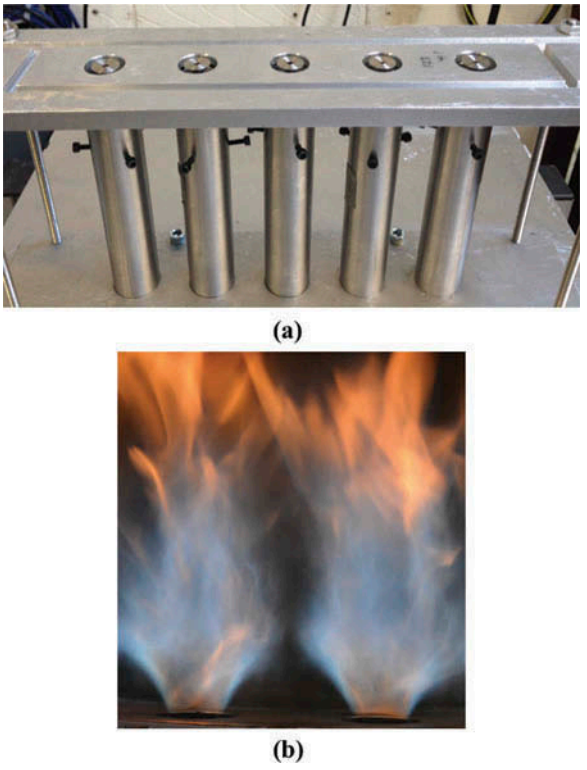

Figure 2. Photographs of the linear non-premixed burner assembly. (a) Side photograph and (b) photograph of flame S1_0.40_10.

velocities at the overall equivalence ratios set in the experiments. To the end of the duct, at the exit of the burner, is attached a conical bluff-body of diameter $Da = 13$ mm, giving a blockage ratio of 50%. Each duct is connected through a 5-mm-diameter flexible tube to a flow divider, the latter being connected to the methane supply. The pipe–bluff-body assemblies are arranged linearly and fixed between upper and lower plates. A six vane, $\alpha = 60^{\circ}$, counter-clockwise swirler (as viewed from the top of the combustion chamber) is fitted 10 mm upstream each of the bluff-body giving a geometrical swirl number of 1.22 (Worth and Dawson, 2013). The combustion chamber is made of rectangular optical-quality quartz plates of 150 mm height and 310 mm and 38 mm length mounted on the top plate, which serves as a chamber backplane. Cartesian coordinates (x, r, z) are chosen with origin at the center of the central burner at the exit of the fuel stream. r is the spanwise coordinate and is chosen along the larger dimension of the rig, whereas x is the cross-stream coordinate.

Two sets of plates were manufactured so that the separation distances between the bluff-body centers are equal to the ones associated with the 12-burner and 18-burner annular configurations from Machover and Mastorakos (2015) corresponding to $S = 2.33D$ (44.0 mm) and $S = 1.56D$ (29.5 mm), called S1 and S2, respectively, where S denotes distance between the bluff-body centers.

Flow conditions

All of the measurements were carried out at ambient conditions of temperature ($T = 293$ K) and pressure (1 atm) for the two spacings mentioned above, at three overall equivalence ratios, and at two bulk velocities. The conditions are summarized in Table 1 and are the same as some of the conditions studied with the annular non-premixed burner studied by Machover and Mastorakos (2015); the Reynolds number, Re, based on the bulk velocity at each burner's annular inlet and D ranged from $Re = 3950$ to $Re = 5400$. The flow rates of air and methane (99.96% purity) were controlled by Alicat mass flow controllers. The flammability limits of the air-CH_4 mixture are $\xi_{lean} = 0.028$ and $\xi_{rich} = 0.089$ with $\xi_{st} = 0.055$ being the stoichiometric mixture fraction (Turns, 2000).

Velocity measurements

The non-reacting cold velocity field in the central burner of the linear rig was measured by one-component laser doppler anemometry (LDA). Air seeded with olive oil particles was passing in the air and the fuel streams with the same flow rates as in the ignition experiments. A Dantec fiber flow LDA system with a Coherent innova series Ar-ion CW laser with a collection angle of 45° was used for the measurements. The optical unit was fitted with a single Bragg cell giving an optical frequency shift of 40 MHz and the receiving optics comprised a lens of focal length 310 mm. Data rates were ranging from 500 Hz to 5 kHz depending on the nature of the flow and the quality of the transmission through the quartz plates. Transmitting and receiving optics were mounted onto a traverse system equipped with stepper motors allowing three-dimensional (3D) translation with 0.1 mm accuracy. The measurements were carried out under different flow conditions and velocity components. Seven axial and radial profiles (full map) covering ranges between $z = 5$ mm and $z = 35$ mm with $z = 5$ mm increment ($z = [5 : 5 : 35]$ mm) were measured for flames S_0.35_10 and S_0.35_14 for the two spacings $S = S1$ and $S = S2$. For flames S1_0.30_10 and S1_0.40_10, axial and radial profiles at $z = [5 : 5 : 15]$ mm were measured, and tangential profiles at $z = [2, 3, 5]$ mm were measured for flame S1_0.35_10. All measurements were covering the radial range $[-S/2, S/2]$ with 0.5-mm increments. Further, 5000 samples were recorded at each measuring location with a minimum validation rate of 80% giving a standard deviation of the sampling distribution less than 1.1% at locations where the root mean square of the velocity is the highest in the measurements.

Table 1. Flow conditions investigated experimentally and numerically for the linear non-premixed burner.

Flame	ϕ	U_{air} (m/s)	U_{CH_4} (m/s)	Remark
S_0.30_10	0.30	9.7	5.9	Effect of decrease in fuel quantity
S_0.35_10	0.35	9.6	6.8	Main case
S_0.40_10	0.40	9.6	7.8	Effect of increase in fuel quantity
S_0.35_14	0.35	13.5	9.6	Effect of air velocity

U_{air} and U_{CH_4} refer respectively to the bulk velocity of the air at the end of the tubes and of the methane at the duct exit. Experimental conditions are tested for the two spacings, $S = S1$ and $S = S2$. A flame characterized by inter-burner spacing S, equivalence ratio ϕ, and bulk velocity U_b is denoted flame $S\_\phi\_U_b$.

Acetone PLIF

The mixture fraction distribution within the central burner of the rig was measured with planar laser-induced fluorescence (PLIF) of acetone. Air seeded with acetone (acetone concentration of approximately 10% by volume, concentration at which effects of laser absorption in the fuel stream can be considered as negligible) was passing in the fuel stream with the same flow rate as in the ignition experiments. This choice was motivated by the perspective to get fuel distribution within the burner representative to that of the ignition experiments.

The laser used was a Surelite Continuum II Nd:YAG laser with a wavelength of 1064 nm pulsed at 10 Hz. At the exit of the laser, the beam power was greater than 80 mJ. Two harmonic crystals were used in series to convert the wavelength first from 1064 nm to 532 nm and then from 532 nm to 266 nm in order to excite the acetone. Beam separators were used to remove the majority of the light of wavelength (532–1064 nm) leaving a beam of 266 nm. Additionally, the laser power was reduced from 6 W to 700 mW through the harmonic crystals and beam separators. A Schott UG5 filter was used to remove any residual light of wavelength 532 nm from the beam. The system comprised a series of lenses forming at the exit a thin laser sheet of 32 mm width and 0.1 thickness. The focus point of this thin sheet was placed at the center line of the central burner of the rig. A 12-bit LaVision Nanostar ICCD detector was used to collect the acetone-fluoresced light in an area corresponding to the three central burners for the two spacing configurations. A Schott WG305 cut-off filter was placed in front of the camera lens to collect the broadband fluorescence signal of acetone (350–550 nm). LaVision's Davis software was used alongside the ICCD and a programmable timing unit was triggering both the laser and ICCD. For *S*1 (respectively *S*2), the area covered was 32×130 mm (respectively 32×100 mm) for an image size of 162×650 pixels (respectively 200×650 pixels), giving a nominal resolution of about 199 μm (respectively 157 μm). For all the cases described in Table 1, 100 images were taken.

The number of counts recorded by the camera is proportional to the density of the acetone within the flow, presently about 5000 in the fuel jet and 0 in the air stream. The mixture fraction is one in the fuel stream where the concentration of acetone is maximum within the flow and is zero in the air stream. For every image, the mixture fraction distribution was then obtained through image corrections. First, dark and background images taken of the flow without acetone were subtracted. The signal-to-noise ratio ranged between 20 and 25 in the present experiments. The raw PLIF images were corrected from the beam profile non-uniformity and the shot-to-shot variation in the laser power by using the instantaneous Dye cell images. The shot noise was then removed from the corrected raw image. Intensity of the pixels of each image was then corrected by comparison with that of the reference image. The latter consisted of the average of 100 images of a laminar jet of air seeded with acetone coming out from the fuel inlet only. Throughout the jet, the mixture fraction was assumed to be equal to 1 everywhere. The intensity was then corrected for each axial location uniformly by dividing the value of the intensity of every pixel by its normalized value in the laminar jet. Note that corrected intensity values of the pixels situated at the lower part of the images ($z \lesssim 4$ mm) was higher than expected for every image. This was due to the reflection of the laser beam on the lower plate of the burner.

Characteristics of the spark

The laser spark was generated by a Continuum Surelite Q-switched Nd-YAG laser operating at 1064 nm. The beam was focused with a 50-mm-diameter biconvex quartz lens of 150-mm focal length. Each pulse of duration 6 ns generated a laser spark at every measurement point in all the flow conditions summarized in Table 1. The 65 mJ of energy delivered was much higher than the minimum ignition energy (6.41 mJ) for methane-air mixtures under atmospheric conditions within the flammability limits (Lewis and Elbe, 1987). In ambient air the size of the plasma generated by each pulse was 3.2 mm and 0.2 mm, respectively, along and perpendicular to the beam path.

Numerical setup

Low-order modeling

Multi-dimensional computational fluid dynamics (CFD) simulations are computationally expensive and the collection of ignition statistics is limited by CPU (central processing unit) cost. Indeed, a large number of initial flow fields is needed in order to ensure proper sampling. Furthermore, complete ignition probability contours requires repeating the procedure at every spark location. Low-order models provide simplified and faster modeling of ignition. They consist in building a model based on a cold flow CFD solution (i.e., without reaction) without need to simulate transient flow. The burner-to-burner propagation was investigated numerically by use of a low-order ignition model introduced first and fully described by Neophytou et al. (2012), in which flame propagation is modeled by the motion of virtual flame particles in a turbulent flow field. The dynamics of the flame particles are modeled by a simplified Langevin model (Pope, 2000) and the algorithm follows a cellular automaton model such that the state of each cell changes over time according to specific rules. Cells can transit through two different states in succession. These are cold state and burned state, and it is not possible for burning cells to go back to the previous cold state. The initial state is cold for all cells and the spark is simulated by switching the cells in the spark volume from the cold to the burned state. When a cell switches its state from the initial cold state to the burned state, it emits a single virtual flame particle whose trajectory follows the Langevin equation. Whenever a virtual flame particle enters a cold cell, the latter switches to the burned state and emits one additional flame particle. In the model, the mixture supply within the combustion chamber and the ignition impact on the cold flow field are not taken into account.

Moreover, an extinction criterion based on the local Karlovitz number (Ka) and originally introduced by Abdel-Gayed and Bradley (1985) is applied to decide whether a flame particle remains active or not. The flame particle quenches if Ka exceeds the critical value $Ka_{crit} = 1.5$. The flammability factor/local mixing is taken into account through the laminar flame speed that is set up to zero when the local mixture is not flammable. In that condition Ka diverges and exceeds the limit set by the extinction criterion resulting in flame particle extinction. The required input for the code to simulate ignition events is a cold flow solution. Neophytou et al. (2012) proposed some criteria based on the turbulent characteristics of the cold flow for the choice of the value of the time step and the grid size. Regarding those guidelines, the retained values were $\Delta x = 0.9$ mm and $\Delta t = 0.5$ ms. From the size of laser spark along the beam path measured experimentally, a spark diameter of 3.2 mm was chosen for modeling.

Cold flow CFD solution

For the two spacings, all of the cold flow field conditions from Table 1 were computed with LES. The solutions were obtained with *ANSYS Fluent* and the Smagorinsky–Lilly subgrid-scale model with default model constants was adopted. Spatial discretization was set up with least square cell-based gradient reconstruction, second-order upwind momentum, and second-order mean mixture fraction. A bounded second-order implicit transient formulation was adopted together with the PISO scheme for the pressure-velocity coupling. The computational domain comprised one single burner sector of the rig. The parallelepipedic volume within the enclosure was extended 7 mm upstream the bluff-body surface in the circular tube. The domain was meshed with an unstructured tetrahedral grid refined in the region of the recirculation zone and in the air inlet. The grid for the *S*1 and *S*2 inter-burner spacing configuration comprised 2.2×10^6 and 2.0×10^6 cells corresponding to 3.7×10^5 and 3.3×10^5 nodes, respectively, with a minimum size of 0.1 mm and a maximum size of 0.5 mm. At the exit of the air inlet, the tangential component of the flow induced by the swirl was set equal to the axial one, following the velocity field measurement presented in the next section. For each case, the CPU time required by the desktop machine used (8 CPUs, Intel R Core TM i7-4820K @3.70 Ghz, 32 GB RAM) was about 50 h. Given the periodicity of the linear burner configurations and for the purpose of reducing the computational cost, the single burner sector had periodic boundary conditions on its walls at half inter-burner distance. For the use of the cold flow field as an input in the low-order model, the CFD solution was interpolated on a regular grid of 0.9-mm spacing and the full rig was constituted by concatenating the five interpolated units through a Matlab procedure. The CPU time required to compute a full-ignition probability map with the low-order model was about 4 h with a desktop PC.

Results and discussion

In this section, results are presented and discussed. Velocity field is first discussed followed by measurements of the mixture fraction. Ignition leading to burner-to-burner propagation is investigated experimentally and then numerically with the low-order ignition model.

Flow field

A photograph of two ignited burners in the non-premixed linear chamber is shown in Figure 2. Each flame is attached to the bluff-body. The flames expand and merge in the region between burners and impinge on both large walls of the combustion chamber.

Measurements of the axial (U_z), radial (U_r), and tangential (U_θ) velocity in the central burner of the rig were obtained in order to get the flow structure and a quantification of the turbulent strain rate within the flow, using the LDA technique described above. Radial profiles at six axial distances from the bluff-body of the mean and root mean square (r.m.s.) of the axial and radial components of the velocity are shown in Figure 3 for flame S1_0.35_10. Figures 3a and 3c depict radial profiles at several axial locations of the mean and r.m.s of the axial velocity. The measurements show a good degree of flow symmetry at every axial distance. The highest axial velocities at $z = 5$ mm are found in the $\pm [8, 14]$ mm

radii corresponding to the wide angle flow coming out from the burner air inlet. Except for a thin area along the axis at $r = \pm 2$ mm corresponding to the central jet of gas characterized by positive axial velocities, the zone situated within the annular air inlet is characterized by negative axial velocities at every axial location, indicating the presence of a central recirculation zone (CRZ). The maximum measured values of the axial velocities in the air inlet and in the gas jet are $1.0U_b$ and $0.6U_b$, respectively, results consistent with the values given in Table 1. Increasing axis location is accompanied by annular air inlet radial expansion with a decrease in positive axial velocities. Likewise, the axial velocity of the central jet decreases up to a distance of approximately 20 mm from the bluff-body, corresponding to the end of jet penetration in the CRZ. The minimum value of the axial velocity in the CRZ reaches $-0.3U_b$ at an axial distance comprised between $z = 10$ mm and $z = 15$ mm. The r.m.s. of the axial velocity peaks when shearing generated by gradients of velocity is large. These gradients are localized at the boundary between the annular air inlet and the CRZ and across the region formed by the zone of penetration of the central jet in the CRZ where intense mixing occurs. Above $z = 25$ mm, the turbulence is rather uniform.

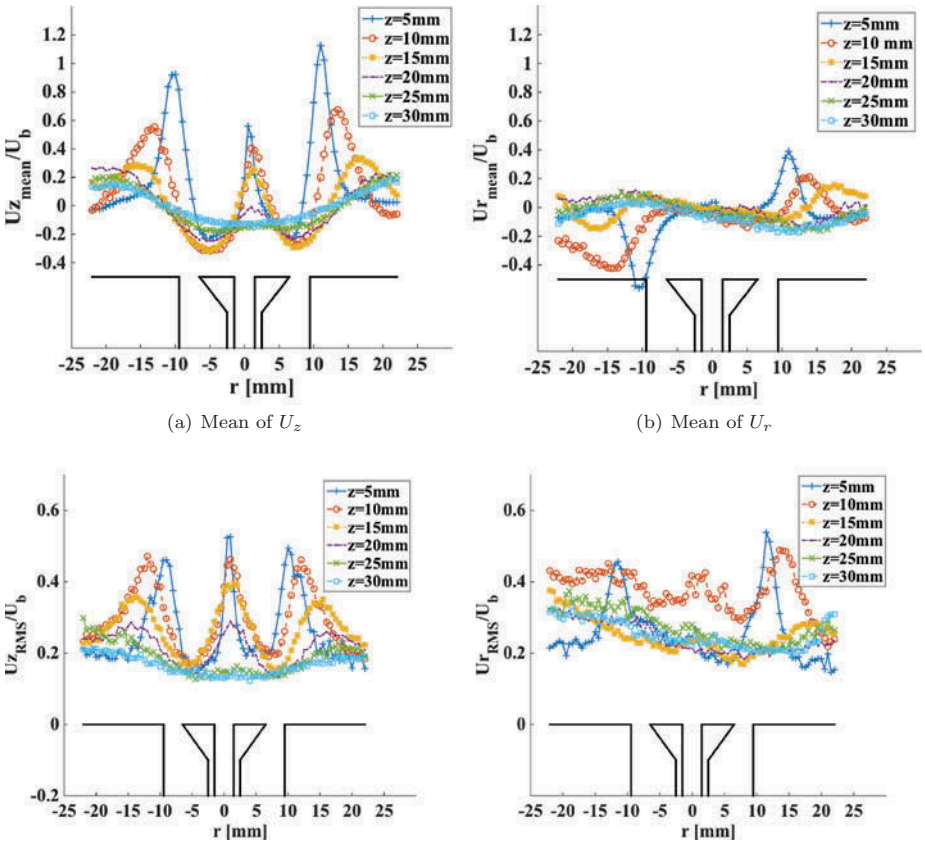

(a) Mean of U_z (b) Mean of U_r

(c) r.m.s. of U_z (d) r.m.s. of U_r

Figure 3. Mean and r.m.s. of the axial component, (a) and (c) respectively, and radial component, (b) and (d) respectively, of the velocity for flame $S1\_0.35\_10$. All profiles are normalized by the bulk velocity U_b. A sketch of a single burner, $r = [-S1/2, S1/2]$ is represented.

Figures 3b and 3d depict radial profiles at several axial locations of the mean and the r.m.s. of the radial velocity. As expected, the flow is antisymmetric with respect to the central axis of the burner. At $z = 5$ mm, the radial velocity has a maximum absolute value of $0.5U_b$ in the zone corresponding to the annular air inlet downstream the edge of the bluff-body. The radial expansion of the air inlet when increasing axial distance is accompanied by a decrease in radial velocity until the profiles become almost uniform for axial locations above 20 mm. At the middle of the inter-burner distance, radial velocity attains zero for axial locations above 20 mm indicating that the adjacent annular jets are merging above that height. The r.m.s. of the radial velocity peaks in the shear layer at the boundary between the air inlet and the CRZ, which is consistent with values of radial velocity close to zero in the central jet and in the CRZ. For values of $z \geq 15$ mm, the r.m.s. profiles are almost uniform with an average r.m.s of $0.3U_b$, which is consistent with previous bluff-body flames measurements (Ahmed et al., 2007a; Cavaliere, 2013).

The tangential component of the velocity has been measured at three axial locations (Figure 4). Avoiding reflections of the laser beam on the lower plate of the burner limited the axial location at a minimum of $z = 2$ mm. The swirl induces an anti-clockwise tangential velocity component in the flow coming out from the air inlet. At $z = 2$ mm, the tangential velocity peaks at a value very close to the bulk velocity U_b and diminishes as the flow coming out from the air inlet expands radially. Inside the CRZ downstream the bluff-body, the flow is characterized by no swirl. The r.m.s of the tangential velocity peaks at the boundary between the annular expanding air flow and the CRZ, similar to the r.m.s. of the radial velocity profiles, as seen by comparing Figures 3d and 4b.

Changes in inter-burner spacing were explored by comparing flames S1_0.35_10 and S2_0.35_10. Velocity profiles of flames S1_0.35_10 (Figure 3a) and S2_0.35_10 (Figure 5a) show that reducing spacing between burners at fixed overall equivalence ratio and bulk velocity, does not change main characteristics of flow. However, at fixed radial position, values of the axial velocity component of the flow coming out from the annular burner air inlet increase slightly with inter-burner spacing reduction. Positive axial velocity values have also been measured at axial distances greater than 30 mm. These measurements

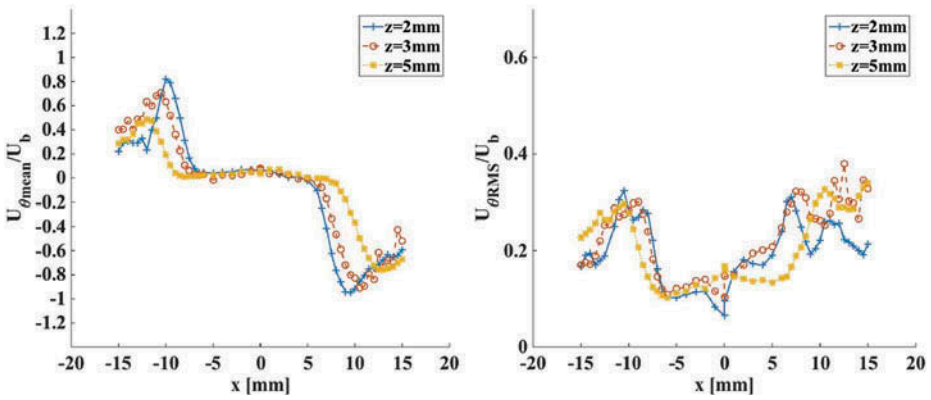

(a) Mean of U_θ (b) r.m.s of U_θ

Figure 4. Mean and r.m.s. of the tangential component of the velocity, (a) and (b) respectively, for flame *S*1_0.35_10. All profiles are normalized by the bulk velocity U_b.

evidence narrowing and shortening CRZ with decreasing inter-burner spacing. Moreover, the height of fuel penetration within the CRZ is reduced with a decrease of S ($z = 10$ mm for flame S2_0.35_10 compared to $z = 20$ mm for flame S1_0.35_10). Reduction of S is accompanied by central jet of gas velocity decrease. Possibly, this difference is due to the same amount of gas recirculated within reduced CRZ volume, favoring mixing between air and gas. As for the axial component of velocity, radial velocity profiles are similar in the $S1$ and $S2$ inter-burner spacing configurations. In the smaller inter-burner spacing configuration, radial velocity is zero in the middle of the inter-burner distance for z above 15 mm, which shows that the adjacent flames merge at a lower height.

Axial velocity profile comparison between flames S2_0.35_10 (Figure 5a) and S2_0.35_14 (Figure 5b) show that are increase in U_b, at fixed ϕ and S, leads to similar profiles when normalizing mean axial velocity by bulk velocity. Results show that flow is Reynolds-number independent for the range of velocity tested, which is consistent with those found for similar bluff-body flows as presented in Cavaliere (2013).

Change in overall equivalence ratio has been investigated, at fixed S and U_b, by increasing ϕ to 0.40 as shown in Figure 6 for flame S1_0.40_10. Increase in ϕ leads to higher speed and penetration of the central jet in the CRZ. Apart from the central jet region, the flow is similar to that for flame $S1$_0.35_10. Similarly, decreasing ϕ to 0.30 results in lower speed and CRZ penetration of the central jet.

Mixture fraction distribution

Measurements of mixture fraction distribution within the combustor have been obtained for all flames presented in Table 1 with the acetone PLIF technique described above. Mean and r.m.s. of the mixture fraction are shown in Figure 7 for flame S1_0.35_10. As expected, the mixture fraction is very high at the central jet inlet location where the air coming out is seeded with acetone, and progressively decreases with increasing axial location. Above the limit of the zone of penetration of the jet in the CRZ evidenced in

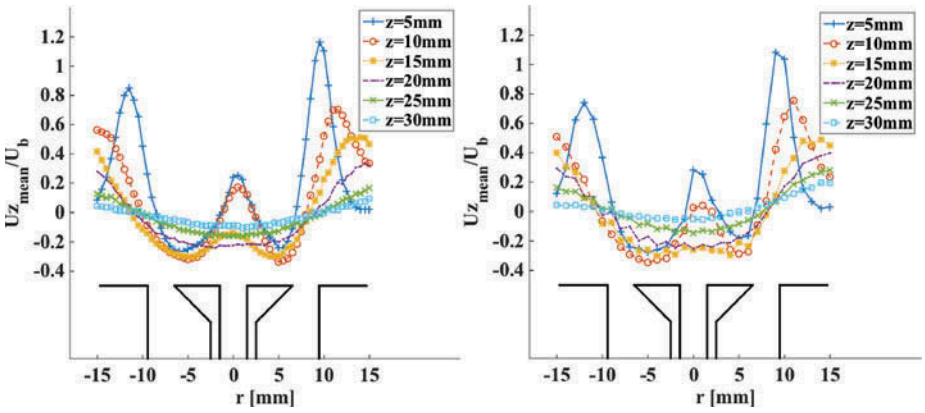

(a) Mean of U_z, S2_0.35_10 (b) Mean of U_z, S2_0.35_14

Figure 5. Axial velocity profiles for flames (a) $S2$_0.35_10 and (b) $S2$_0.35_14. All profiles are normalized by the bulk velocity U_b. A sketch of a single burner, $r = [-S2/2, S2/2]$ is represented.

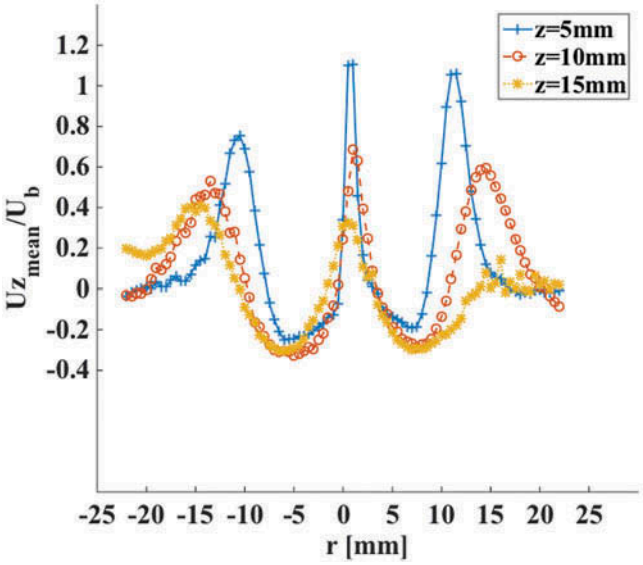

Figure 6. Axial velocity profiles for flame $S1\_0.40\_10$. All profiles are normalized by the bulk velocity U_b.

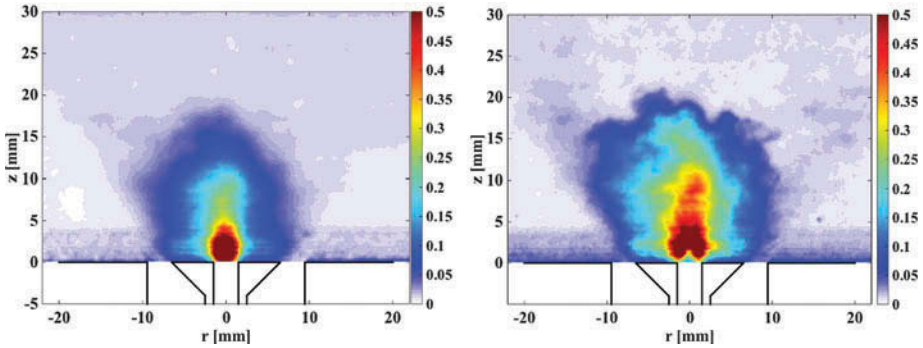

(a) Mean of the mixture fraction (b) r.m.s of the mixture fraction

Figure 7. (a) Mean and (b) r.m.s. of the mixture fraction measurements for flame S1_0.35_10. Background correction is applied.

the velocity measurements, no more mixing occurs and mixture fraction is rather uniform. The fuel-air mixture concentrates in the region expanding radially within the limits of the flow coming out from the burner air inlet. Immediately downstream the fuel inlet, where $\xi = 1$, r.m.s. of the mixture fraction is low. With increasing axial location within the jet, the r.m.s. suddenly increases forming a cone within the jet delimiting the zone of mixing, and then gradually decreases as increases the degree of mixing. Mixture fraction r.m.s. is high in the CRZ where air and gas are not fully mixed and is zero above the zone of penetration of the gas in the CRZ where mixture is homogeneous.

Flammability factor contours, calculated by integrating the probability density function of the mixture fraction between ξ_{lean} and ξ_{rich}, are shown for flame S1_0.35_10 in Figure 8.

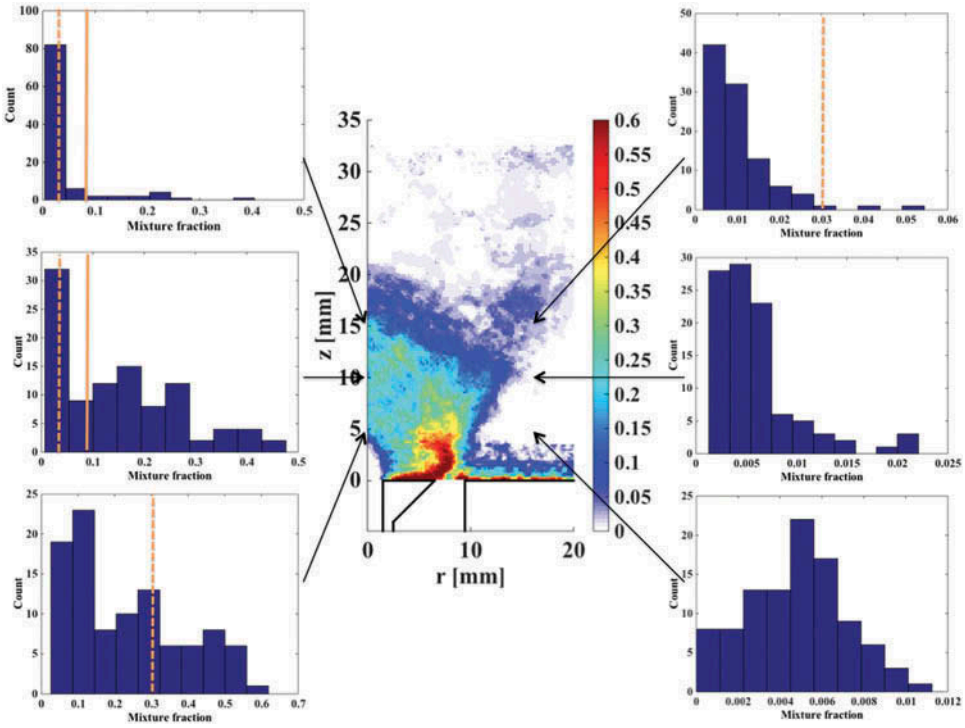

Figure 8. Flammability factor and the PDF of the mixture fraction at several positions for flame S1_0.35_10. The positive values of the flammability factor around $z = 0$ mm are due to the reflection of the beam of the laser on the lower plate of the burner. Lean ($\xi_{lean} = 0.028$) and rich flammability limits ($\xi_{rich} = 0.089$) are represented with dotted and solid lines in the PDF graphs, respectively. A sketch of a half single burner, $r = [0, S1/2]$, is represented.

PDF of the mixture fraction is shown for six distinct locations in one half of the central burner. In the CRZ, F is zero in the neighborhood of the central jet inlet where the mixture is rich, reaches positive values in the zone of highly recirculating flow, and drops back to zero above the zone of penetration of gas within the CRZ where air and gas are fully mixed. For all of the flames studied, the homogeneous mixture fraction ξ_{hom} is smaller than the lean flammable limit ($\xi_{hom} = 0.017$ and $\xi_{hom} = 0.023$ at ϕ = 0.3 and ϕ = 0.4, respectively). Positive, albeit small, values of F ($F \leq$ 5%) are evidenced in the inter-burner region, throughout the annular jets formed by the expanding air flow, showing that the swirling air flow extracts an amount of gas from the CRZ. These positive values indicate the existence of bridges of positive flammability factor in the inter-burner region allowing flame fragments to travel to the next adjacent unignited burner as evidenced by Machover and Mastorakos (2015).

Effects on flammability factor contours of inter-burner spacing and overall equivalence ratio variations were investigated (Figure 9). When reducing spacing between burners, at fixed ϕ and U_b, air and gas mix faster within the CRZ as evidenced by velocity measurements (for flame S1_0.35_10, the length of the zone of penetration within the CRZ is about 20 mm, Figure 3, whereas for flame S2_0.35_10, the length of the zone of penetration within the CRZ is about 15 mm, Figure 5). Furthermore, length of the bridges is

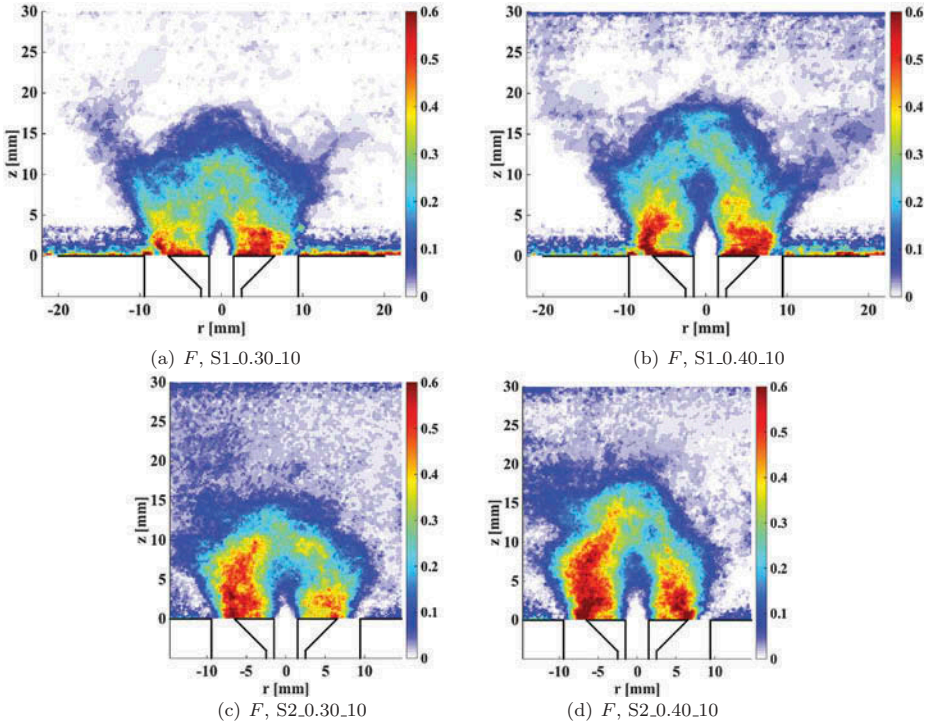

(a) F, S1_0.30_10 (b) F, S1_0.40_10

(c) F, S2_0.30_10 (d) F, S2_0.40_10

Figure 9. Calculated flammability factor maps from experiments for flames (a) S1_0.30_10, (b) S1_0.40_10, (c) S2_0.30_10, and (d) S2_0.40_10. The positive values of the flammability factor around $z = 0$ mm are due to the reflection of the beam of the laser on the lower plate of the burner.

reduced, since adjacent flames merge at shorter axial distance from the bluff-body as inter-burner spacing is reduced. Indeed, bridges of positive flammability factor being situated in the expanding annular air inlet, a flame fragment coming from the CRZ of the ignited burner has a higher probability to penetrate in the CRZ of the next un-ignited burner if flames merge at lower axial distance. For both spacings considered, increase of fuel amount results in axial and radial expansion of the region within the central jet where the flammability factor is null and in that of the zone of positive F in the CRZ. Moreover, flammability factor measured within the bridges increases, leading to higher probability for a flame fragment to survive in the inter-burner region.

Ignition probability measurements

Contours of ignition probability P_{ign} were obtained for all flames considered. In every case, establishment of a stable flame within the burner sparked generated spreading of flame to the adjacent burners. Indeed, it was shown that burner-to-burner flame propagation occurring in the stratified inter-burner region consisted of a successful flame propagation event following a succession of failed events in which a flame fragment coming from the ignited burner failed to penetrate fully in the recirculation zone of the adjacent un-ignited burner (Machover and Mastorakos, 2015). Hence, the burner-to-burner propagation consists in a succession of failed events occurring prior to a successful event leading to

adjacent burner successful ignition. Either the flame is in the stable light-round region (shown experimentally for the three inter-burner spacings in Machover and Mastorakos, 2015) and successful propagation occurs long term, or the flame is beyond the lean light-round ignition limit and the burner-to-burner propagation never occurs. All of the flames studied range in the stable ignition region, which implies that if the first burner is successfully ignited, light-round always occurs in the combustion chamber. Hence, the probability of igniting one burner is equal to the probability of igniting the full combustor. Thus, successful ignition is defined here as a spark event leading to successful burner-to-burner propagation. For each location within the central burner, P_{ign} was determined experimentally by performing $N = 20$ individual laser spark events. Dividing the number of successful ignitions by N resulted in the determination of P_{ign}. In this case, the standard error was $[P_{ign}(1 - P_{ign})/N]^{1/2} = 11\%$ for $P_{ign} = 50\%$.

Regarding the rather good symmetry of the flow, measurements of P_{ign} have been carried out in one half of the central burner. In every case, sparking occurred at 42 different locations across and along the half burner on a plane passing by the burner axes. Six radial locations detailed in Table 2 were sparked at seven axial locations ranging from 5 mm up to 35 mm with 5-mm increments. In order to avoid reflections of the beam by sparking close to the lower plate of the burner, the minimum axial sparking location was chosen at 5 mm.

In order to explore the influence of the mixing field and the flow pattern on probability of ignition, flammability factor (F), normalized axial velocity (U_z/U_b), normalized fluctuation of the turbulent velocity (u'/U_b), and ignition probability contours (P_{ign}) are represented together for flames S1_0.35_10, S2_0.35_10, and S2_0.35_14 in Figures 10, 11, and 12, respectively.

For a 3D velocity field, the magnitude of the fluctuation of the turbulent velocity u' can be estimated as $3u'^2/2 = 1/2(u_{RMS}^2 + v_{RMS}^2 + w_{RMS}^2)$, where u_{RMS}, v_{RMS}, and w_{RMS} denote the r.m.s. of the axial, radial, and tangential velocity, respectively. Assuming isotropy of the turbulence in the planes $z =$ constant, as illustrated by similar r.m.s of the radial and tangential velocity profiles for flame S1_0.35_10 (Figures 3d and 4b), u' can be expressed as $u' = [(u_{RMS}^2 + 2v_{RMS}^2)/3]^{1/2}$. Flammability factor contours and axial velocity maps provide from the acetone PLIF and LDA measurements, respectively.

For flame S1_0.35_10, the ignition probability contours displayed in Figure 10a differ from the flammability factor contours shown in Figure 10b. P_{ign} is small in a thin area along the axis corresponding to the central jet. This low ignition probability zone expands up to a distance of approximately 15 mm from the bluff-body, whereas the region where flammability factor is equal to zero expands until approximately 5 mm. This can be explained by looking at the u'/U_b contours depicted in Figure. 10c that show very high

Table 2. Radial positions for the measurements of P_{ign} at $z = [5 : 5 : 35]$ mm.

Radial position (mm)	Comment
0	$r = 0$; center of the burner
3.25	$r = Da/4$; half radius of the bluff-body
6.50	$r = Da/2$; edge of the bluff-body
9.45	$r = D/2$; edge of the annular air inlet
15.74 (12.10)*	Half distance between the edge of the air inlet and the end of the burner
22.02 (14.70)*	$r = S1/2$ ($r = S2/2$)*; end of the burner

* Values between parentheses correspond to the $S2$ configuration burner.

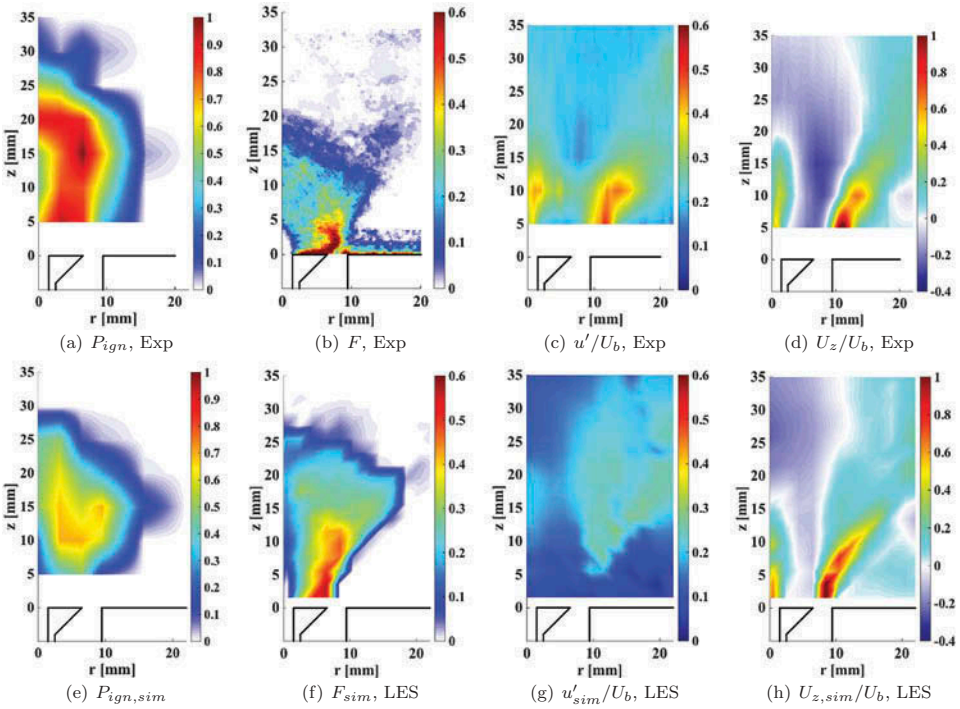

Figure 10. Measurements: (a) probability of ignition, (b) flammability factor, (c) normalized fluctuation of the turbulent velocity, and (d) normalized axial velocity. Simulation: (e) probability of ignition. LES: (f) flammability factor, (g) normalized fluctuation of the turbulent velocity, and (h) normalized axial velocity. Flame S1_0.35_10. A sketch of a single burner, $r = [0, S1/2]$, is represented.

strain rate in the central jet region until approximately 15 mm. This decrease in P_{ign} is consistent with previously reported experimental and numerical studies (Ahmed et al., 2007a; Richardson and Mastorakos, 2007). Furthermore, the region of high P_{ign} corresponding to nearly the whole CRZ of the burner is much wider than the zone of high flammability factor evidenced previously. P_{ign} is greater than F nearly everywhere within the burner, gap between these values being particularly large in regions of negative axial velocity as shown in Figure 10d. These differences can be attributed to non-local effects, such as convection of the kernel towards the center of the recirculation zone, where the values of F are high, supporting therefore the analysis from Ahmed et al. (2007a). P_{ign} has been found to be less than 5% in the bridges of positive flammability factor located in the inter-burner region where kernels are subject to high axial velocities and are not captured by the CRZ of the sparked burner. Hence, the results obtained are consistent with small values of F measured in the inter-burner region. These results confirm that both flammability factor and flow pattern are important to predict ignition, as reported previously for single burners (Ahmed et al., 2007a, Ahmed et al., 2007b, Ahmed and Mastorakos, 2006).

Effects of varying overall equivalence ratio at fixed inter-burner spacing and bulk velocity on the ignition contours were investigated as shown in Figures 15 and 16. Increasing overall equivalence ratio results in axial and radial expansion of the region with high P_{ign} within the CRZ, following the trends observed for F in Fig. 9, and consistent

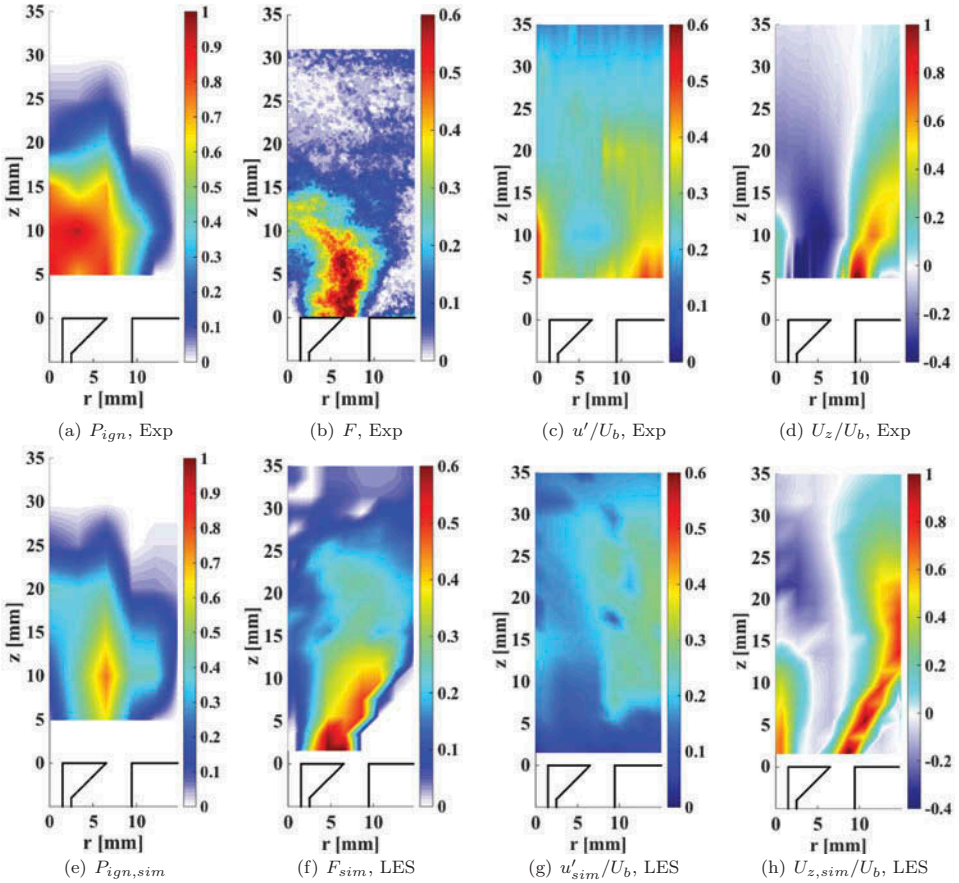

Figure 11. Measurements: (a) probability of ignition, (b) flammability factor, (c) normalized fluctuation of the turbulent velocity, and (d) normalized axial velocity. Simulation: (e) probability of ignition. LES: (f) flammability factor, (g) normalized fluctuation of the turbulent velocity, and (h) normalized axial velocity. Flame S2_0.35_10. A sketch of a single burner, $r = [0, S2/2]$, is represented.

with the results obtained in Ahmed et al. (2007a). Similarly, decreasing flammability factor value results in expansion of the zone of low P_{ign} within the central jet of gas. Positive values of P_{ign} obtained where $F = 0$ can be explained by downstream convection of the kernel by the jet until it reaches the recirculating flow characterized by higher values of F.

Influence of decrease in inter-burner spacing on P_{ign} was investigated by comparing ignition probability contours obtained for flame S1_035_10 (Figure 10a) with those obtained for flame S2_035_10 (Figure 11a). Decrease in inter-burner spacing results in reduction of height of the zone of high P_{ign} within the CRZ. However, high values of P_{ign} remain in the central jet despite $F = 0$ (Figure 11b), and high strain rate (Figure 11c). This result may be seen as the consequence of better degree of mixing between air and gas evidenced by the flow field measurements.

At fixed inter-burner spacing and overall equivalence ratio, increase of bulk velocity from 10 m/s to 14 m/s results in decrease of P_{ign} (Figure 12a) even in locations of favorable negative air velocities (Figure 12d). These results are consistent with similar trends previously observed

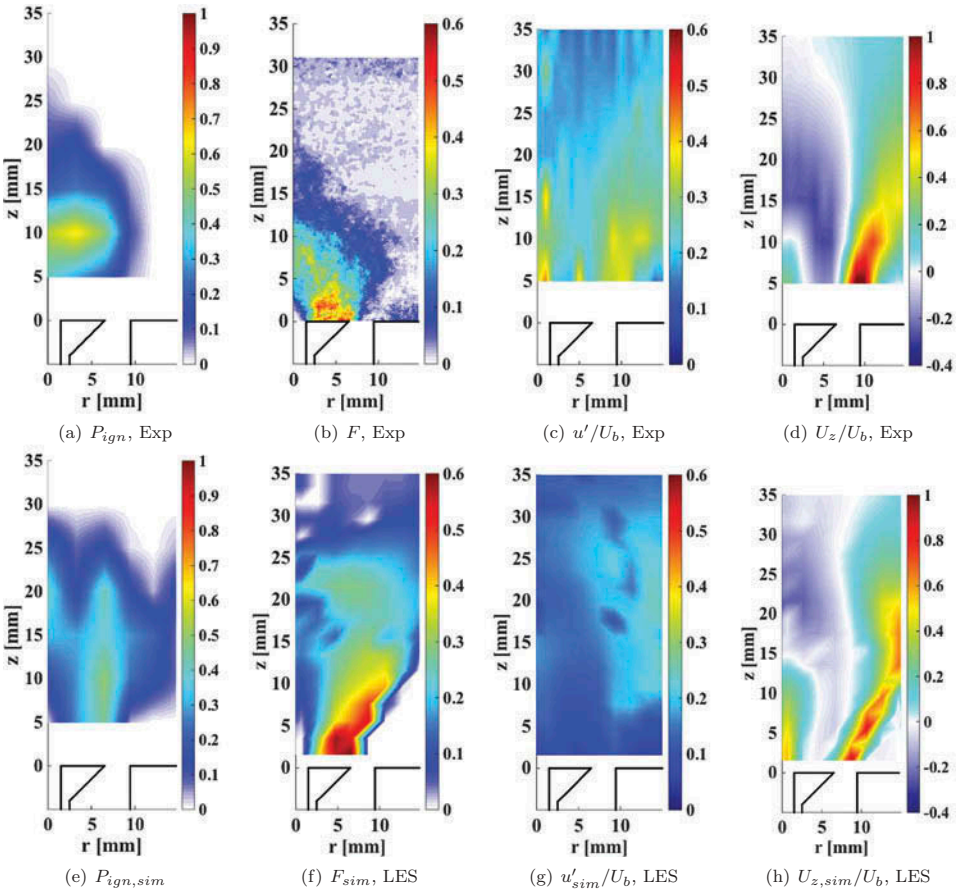

Figure 12. Measurements: (a) probability of ignition, (b) flammability factor, (c) normalized fluctuation of the turbulent velocity, and (d) normalized axial velocity. Simulation: (e) probability of ignition. LES: (f) flammability factor, (g) normalized fluctuation of the turbulent velocity, and (h) normalized axial velocity. Flame S2_0.35_14. A sketch of a single burner, $r = [0, S2/2]$, is represented.

(Ahmed et al., 2007a; Ahmed and Mastorakos, 2006) and are attributed to higher strain rate everywhere in the flow as evidenced by comparing u'/U_b values plotted in Figures 11c and 12c. At high bulk velocity, ignition probability has positive values in the CRZ, and in the neighborhood of the central jet where the highly recirculating flow favors mixing between air and gas. In this case, P_{ign} is always smaller than 5% in the inter-burner zone.

Modeling results

Simulated ignition probability contours ($P_{ign,sim}$) were obtained numerically with the low-order ignition model described above for all flames in Table 2. Successful ignition is again defined as a spark event leading to successful burner-to-burner flame propagation. However, contrary to the experiments, successful burner ignition does not always result in spreading among adjacent burners. The numerical study investigates the full combustor since successful ignition of one burner does not result necessarily in full burner propagation. Here, light-round

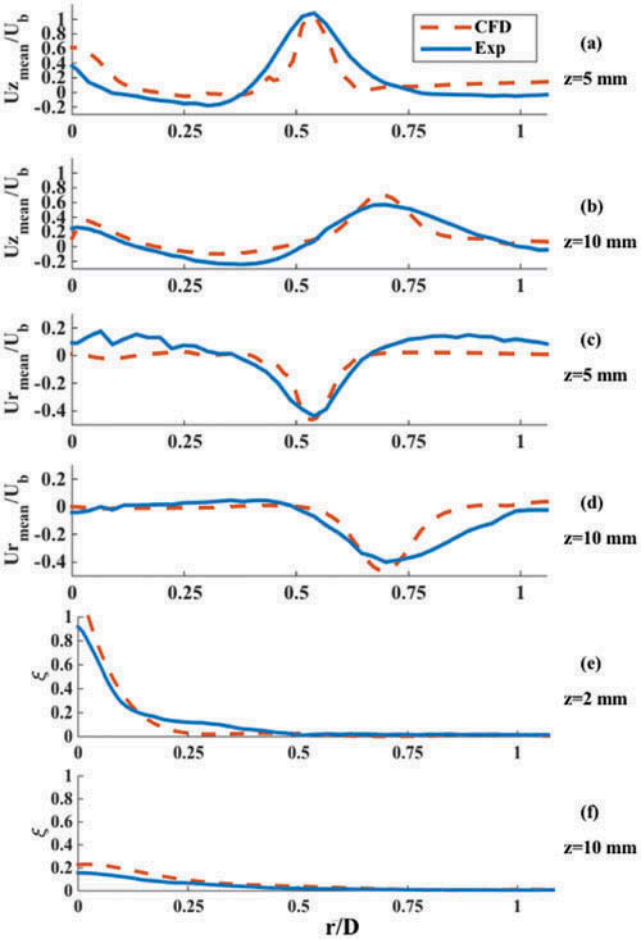

Figure 13. Comparison between experimental axial and radial velocity profiles (solid line) and CFD (dotted line) for flame $S1\_0.30\_10$. (a) Axial component at $z = 5$ mm. (b) Axial component at $z = 10$ mm. (c) Radial component at $z = 5$ mm. (d) Radial component at $z = 10$ mm. (e) Mean of the mixture fraction at $z = 2$ mm. (f) Mean of the mixture fraction at $z = 10$ mm. Half burner ($r = [0, S1/2]$). All profiles are normalized by the bulk velocity U_b.

is considered successful if at least one burning virtual particle emitted from the sparked central burner penetrates in an adjacent one. For that purpose, the rig has been split into sectors corresponding to the individual burners. $P_{ign,sim}$ was determined by performing 50 individual spark events. In this case, standard error was 7.5% for $P_{ign,sim} = 50\%$.

Cold flow

The cold flow fields obtained with LES were validated by comparing simulated mean axial velocity, radial velocity, and mean mixture fraction profiles with experiments at two axial locations for flame S1_0.30_10 (Figure 13). LES captures accurately the three zones characteristic of the flow topology: central jet, CRZ, and expanding annular flow coming out from the burner air inlet. Furthermore, the magnitude of the time-averaged axial and

radial velocity components suitably follow experimental data, showing that the convective pattern within the burner is well captured by the LES. Moreover, the mean mixture fraction profiles obtained with LES agree reasonably well with that measured with the acetone PLIF technique. The mean mixture fraction is close to 1 at small axial locations and decreases as the gas jet penetrates in the CRZ.

Flammability factor contours obtained numerically for flames 12_0.35_10, 18_0.35_10, and 18_0.35_14 are shown in Figures 10f, 11f and 12f, respectively. The main characteristics evidenced experimentally are retrieved in the LES. These are (i) zero F in central jet of gas and outside the zone delimited by the flow coming out from the burner air inlet, and (ii) high F downstream the bluff-body where fuel and air mix together within the CRZ. Bridges of small flammability factor are present in the inter-burner region. Reducing inter-burner spacing results in axial expansion of the zone of high F_{sim} and in reduction of the length of bridges, as seen by comparing Figure 10f and 11f, which increases the probability for a flame fragment to travel successfully from burner to burner. The discrepancies between simulated contours and their experimental counterparts may result from the periodic boundary conditions adopted for the LES. In a linearly arranged configuration an infinite number of injectors is mimicked, resulting in air entrainment changes and bulk rotational motion appearance within the combustor, originating from the addition of the swirling flows of each individual burner as evidenced in Barré et al. (2014).

Flame propagation pattern

The burner-to-burner propagation mechanism is visible in Figure 14, where a successful flame propagation from burner to burner (from the center burner to that on the right) and a failed burner-to-burner propagation (from the center burner to that on the left) are shown for flame S2_0.40_10. The central burner is sparked at position ($x = 0$ mm, $r =$ 6.25 mm, $z = 15$ mm). First, a downstream propagation is visible until the CRZ of the sparked burner has ignited ($t = 30$ ms). Then, the flame propagates along a flammable bridge between the sparked burner and the left adjacent one until the ignited flame particles (represented in green) have quenched at $z \approx 40$ mm ($t = 37.5$ ms). This corresponds to a failed event. Successful burner-to-burner flame propagation consists in a flame fragment coming from the ignited burner that travels successfully in the inter-burner region at $z \approx 25$ mm along a bridge of positive flammability factor (between $t = 67.5$ ms and $t = 75$ ms) until it is convected upstream by the recirculation zone (RZ) of the adjacent un-ignited adjacent burner ($t = 82.5$ ms). The RZ of the latter ignites then successfully ($t = 90$ ms) leading to full ignition of the burner ($t = 105$ ms). These results show that the light-round mechanisms described in Machover and Mastorakos (2015) are well retrieved by the low-order ignition model adapted to a full combustion chamber.

Ignition probability modeling

Simulated ignition probability contours obtained with the low-order model, flammability factor (F_{sim}), normalized axial velocity ($U_{z,sim}/U_b$), and normalized fluctuation of the turbulent velocity (u'_{sim}/U_b), obtained with LES are displayed together with the experimental data for flames S1_0.35_10, S2_0.35_10, and S2_0.35_14 in Figures 10, 11, and 12,

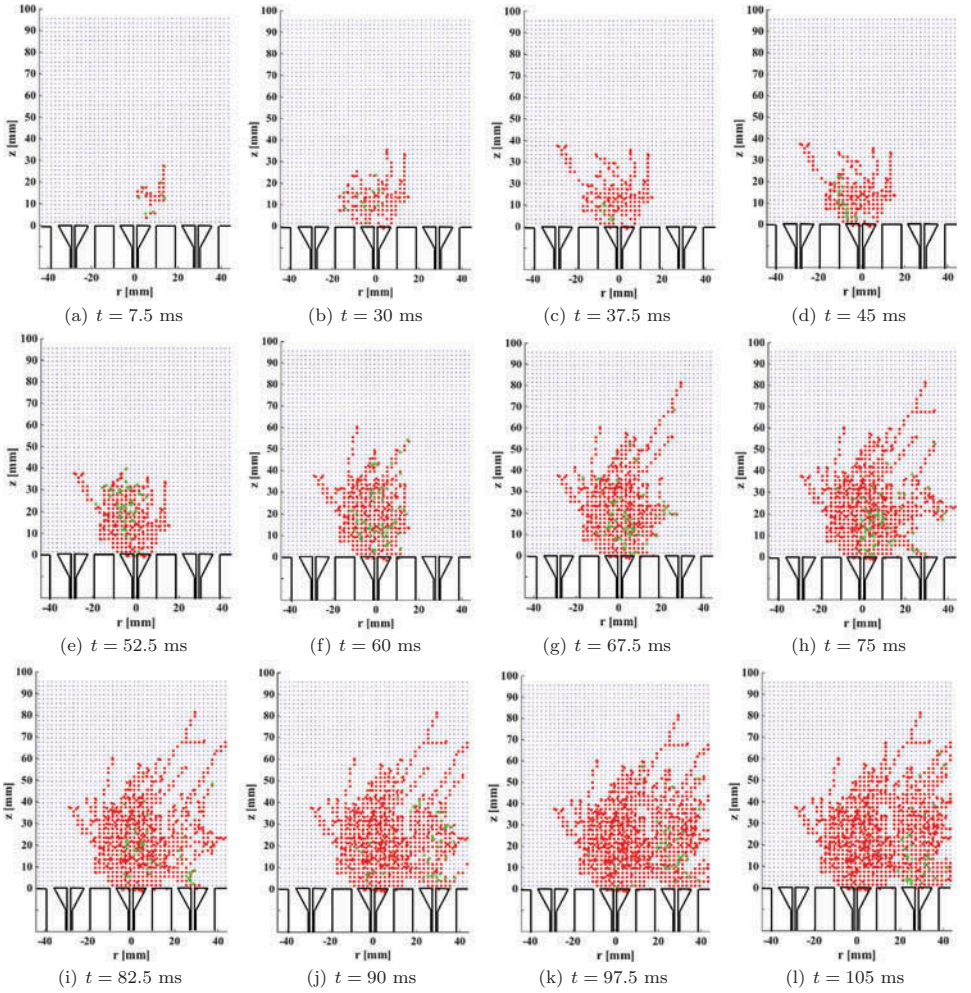

(a) $t = 7.5$ ms (b) $t = 30$ ms (c) $t = 37.5$ ms (d) $t = 45$ ms

(e) $t = 52.5$ ms (f) $t = 60$ ms (g) $t = 67.5$ ms (h) $t = 75$ ms

(i) $t = 82.5$ ms (j) $t = 90$ ms (k) $t = 97.5$ ms (l) $t = 105$ ms

Figure 14. Simulated front view visualization of successful burner ignition (from middle to right) and failed burner ignition (from middle to left) during one spark ignition event. Flame S2_0.40_10. Cold cells, burning particles, and extinguished particles are represented in blue, green, and red, respectively. A sketch of three single burners, $r = [-3.S1/2, 3.S1/2]$, is represented.

respectively. For all simulations, the dependency to the local flow composition was included and the laminar flame speed was determined according to the local equivalence ratio (Vagelopoulos and Egolfopoulos, 1998).

Simulated ignition probability contours and flammability factor contours obtained with LES are shown for flame S1_0.35_10 (Figure 10e and 10f, respectively) and for flame S2_0.35_10 (Figures 11e and 11f, respectively). For both inter-burner spacing configurations, the higher values of $P_{ign,sim}$ are found to be within the CRZ, where the flow recirculates with high values of F_{sim}, a result consistent with the experimental measurements. Decrease of $P_{ign,sim}$ occurs in the central jet region where F_{sim} is close to zero. Similarly to experimental results, $P_{ign,sim}$>F_{sim} in central jet region, which is explained by

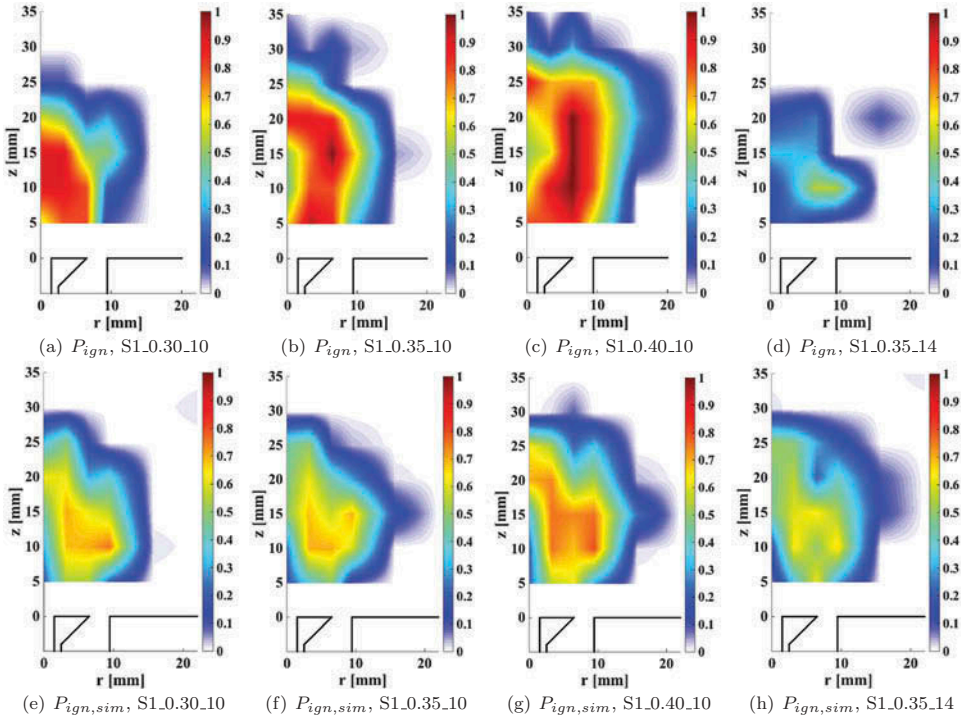

(a) P_{ign}, S1_0.30_10 (b) P_{ign}, S1_0.35_10 (c) P_{ign}, S1_0.40_10 (d) P_{ign}, S1_0.35_14

(e) $P_{ign,sim}$, S1_0.30_10 (f) $P_{ign,sim}$, S1_0.35_10 (g) $P_{ign,sim}$, S1_0.40_10 (h) $P_{ign,sim}$, S1_0.35_14

Figure 15. Probability of ignition contours measured (P_{ign}) and calculated with the low-order code SPINTHIR ($P_{ign,sim}$) in the 12-burner configuration. A sketch of a half single burner, $r = [0, S1/2]$, is represented.

kernel convection by the jet and their capture by the recirculating flow. Positive values of ignition probability found in the bridges of positive flammability factor in the inter-burner zone reflect the ability to capture less probable ignition events with increasing number of spark events.

Effects of varying inter-burner spacing, overall equivalence ratio and bulk velocity on the ignition probability were investigated as shown in Figures 15 and 16. The trends observed are the same as in the experiments. Increase in ϕ results in axial and radial expansion of the zone of high $P_{ign,sim}$ within the CRZ and higher values of $P_{ign,sim}$ in the inter-burner region. Increase in U_b leads to decrease of ignition probability at every location. In every case, regions of highest ignition probability are located where air and gas mix together within the CRZ, between the radial gas jet and the expanding air inlet.

These results show that for all flames studied, ignition probability variations within the burner are accurately captured by the low-order ignition model. However, at every location, values of ignition probability obtained with the ignition model are lower than that measured by experiments. The gap between experimental and numerical ignition probabilities is large in the recirculation zone and very small outside the CRZ. These results are explained by burner refueling as follows. If one supposes a spark is applied at location x in the first burner denoted B_1 and lets denote by $P_{B_{1,x}}$ the probability that the spark kernel leads to successful ignition of B_1. Similarly, lets denote by $P_{B_{2,x}}$ the probability that the same spark kernel leads to successful

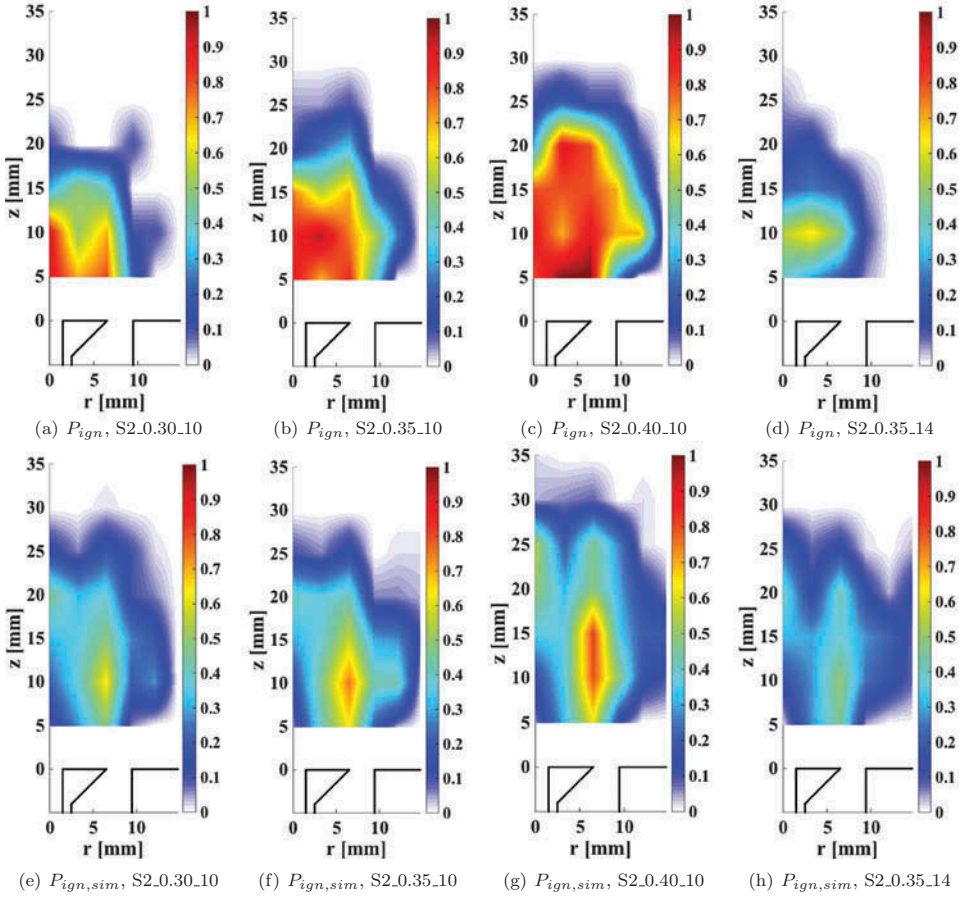

Figure 16. Probability of ignition contours measured (P_{ign}) and calculated with the low-order code SPINTHIR ($P_{ign,sim}$) in the 18-burner configuration. A sketch of a half single burner, $r = [0, S2/2]$, is represented.

ignition of the second burner denoted B_2, such that B_2 is the adjacent burner closest to the spark. Successful burner-to-burner propagation, i.e., successful ignition of B_2, occurs in two possible ways. Either sparking within B_1 results in direct ignition of B_2 or results in ignition of B_1 that subsequently ignites B_2. Let $P_{1,2}$ be the probability (supposed to be dependent on S, ϕ, and U_b) that during a single ignition full event flame propagates from one burner to the adjacent one. In one case with refueling, B_1 stays always ignited and leads necessarily to long-term flame propagation from B_1 to B_2 such that $P_{1,2} = 1$. Hence, with refueling, the probability of ignition at location x is $P_{ign,x,fuel} = sup(P_{1,2}.P_{B_{1,x}}, P_{B_{2,x}}) = sup(P_{B_{1,x}}, P_{B_{2,x}})$. In the other case without refueling, the sparked burner extinguishes in the long-term since $F < 1$ in every location. Indeed, the code has no "memory" of the burning state of the burner since a grid cell that has extinguished cannot go back to its former ignited state. Hence, successful ignition of B_1 does not lead necessarily to ignition of B_2, i.e., $P_{1,2} \leq 1$. Therefore, without refueling probability of ignition at location x is $P_{ign,x,nofuel} = sup(P_{B_{1,x}}.P_{1,2}, P_{B_{2,x}}) \leq sup(P_{B_{1,x}}, P_{B_{2,x}}) = P_{ign,x,fuel}$. These results explain the lower values of $P_{ign,sim}$ obtained numerically since the low-order model does

not take into account burner refueling. Furthermore, when sparking within the CRZ of the first burner, the flame kernel has a low probability to ignite B_2, and a high probability to ignite B_1. The latter leads to flame propagation with probability $P_{1,2} = 1$ in case of refueling and $P_{1,2} \leq 1$ in the absence of refueling. Here, we have $P_{ign} \approx P_{B_{1,x}}.P_{1,2}$, which explains that in the CRZ, values of P_{ign} obtained with the ignition model are smaller than that measured with experiments. However, when sparking within the bridges of positive flammability factor in the inter-burner area, where axial and radial velocity components are positive, the kernel has a low probability to ignite B_1. Hence, $P_{ign} \approx P_{B_{2,x}}$, which explains that in the inter-burner region, values of P_{ign} obtained numerically are very close to that measured experimentally.

The present results indicate as possible improvements of the low-order model that the mixture supply within the combustion chamber (i.e., extinguished cells could be able to switch back to their cold state) and that the ignition impact on the cold flow field could be considered.

Conclusions

A new rig consisting of a series of bluff-body swirl non-premixed burners arranged linearly, based on an annular non-premixed burner previously developed at University of Cambridge, has been examined in order to understand the light-round mechanism, namely, the way a flame propagates from one burner to the next adjacent one. The rig consists of a series of repeatable sectors associated to each individual burner, one being the image of the other by translation of the inter-burner spacing. The study has been conducted by varying inter-burner spacing, overall equivalence ratio, and bulk velocity.

LDA velocity measurements have shown that the Reynolds number independent flow, in the range of *Re* investigated, is characterized by a central jet and a central recirculation zone comprised in the region delimited by the flow coming out from the burner air inlet. Results showed that increasing overall equivalence ratio expands the zone of penetration of the gas within the recirculation zone without changing flow features elsewhere. Furthermore, reducing inter-burner spacing results in faster air-gas mixing.

PLIF of acetone has been used in order to measure the mixture fraction distribution within the combustion chamber. Measurements showed high values of mean and r.m.s. of the mixture fraction in the central jet of pure gas where the mixture is not flammable. In the CRZ, high values of flammability factor were measured, especially between the jet of gas and the expanding air flow where strong mixing occurs. In the inter-burner region, bridges characterized by positive, albeit small, flammability factor allow successful propagation of flame fragment from one ignited burner to the next non-ignited one, leading to its successful ignition. These bridges are located throughout the expanding air inlet, showing that air flow extracts an amount of gas from the CRZ. Increasing overall equivalence ratio results in axial and radial expansion of the zone of high flammability factor within the CRZ and in higher values of flammability factor in the inter-burner region. Diminishing the spacing between burners results in reduction of the bridge lengths since the flames merge at smaller axial distance in the inter-burner region.

Contours of ignition probability P_{ign}, defined here as the probability that a spark event generates burner-to-burner propagation, have been obtained by sparking several times

with a laser at various locations within the flow. The contours showed that the highest P_{ign} are located in the CRZ in regions characterized by high flammability factor and negative axial velocities. Moreover, values of P_{ign} are consistent with the values of flammability factor obtained in the inter-burner bridges. Differences between values of ignition probability and flammability factor have been interpreted as the result of non-local effects, such as convection and local quenching.

Finally, ignition probability contours have been obtained using a stochastic low-order ignition model adapted to the present non-premixed linear configuration. Simulations were performed in the entire combustion chamber and the ignition model was able to capture the variations of ignition probability with changes of spark locations and flow parameters. However, the values obtained have been found to be considerably smaller than those measured, especially in the CRZ. Studying qualitatively the probability that sparking within a burner results in ignition of the adjacent one, with regard to refueling or not refueling the burner with fresh air-gas mixture, explained the differences observed between experiments and simulations.

Consequently, in the present non-premixed configuration, each ignited burner acts as a reservoir of hot products. Burner-to-burner propagation occurs as soon as a flame fragment travels from the recirculation zone of the ignited burner to the recirculation zone of the adjacent non-ignited one. Successful propagation is made possible by the existence of bridges of positive, albeit small, flammability factor in the inter-burner region. Refueling is essential for successful propagation given that the very small values of flammability factor measured in the bridges allow only a small fraction of the flame fragments to penetrate in the adjacent un-ignited burner.

The present results can be useful to understand the underlying physics behind the global behavior of annular non-premixed combustors.

Acknowledgments

The authors wish to thank Drs. J. Kariuki, M. Kotzagianni, and D. Farrow for assistance with the experimental measurements.

Funding

The authors gratefully acknowledge financial assistance from the EPSRC.

ORCID

Epaminondas Mastorakos http://orcid.org/0000-0001-8245-5188

References

Abdel-Gayed, R., and Bradley, D. 1985. Criteria for turbulent propagation limits of premixed flames. *Combust. Flame*, **62**, 61–68.

Ahmed, S., Balachandran, R., Marchione, T. and Mastorakos, E. 2007a. Spark ignition of turbulent nonpremixed bluff-body flames. *Combust. Flame*, **151**, 366–385.

Ahmed, S., Balachandran, R., and Mastorakos, E. 2007b. Measurements of ignition probability in turbulent non-premixed counterflow flames. *Pro. Combust. Inst.*, **31**, 1507–1513.

Ahmed, S., and Mastorakos, E. 2006. Spark ignition of lifted turbulent jet flames. *Combust. Flame*, **146**, 215–231.

Ahmed, S., and Mastorakos, E. 2010. Correlation of spark ignition with the local instantaneous mixture fraction in a turbulent nonpremixed methane jet. *Combust. Sci. Technol.*, **182**, 1360–1368.

Ahmed, S., and Mastorakos, E. 2016. Spark ignition of a turbulent shear-less fuel-air mixing layer. *Fuel*, **164**, 297–304.

Barré, D., Escalpez, L., Cordier, M., Riber, E., Cuenot, B., Staffelbach, G., Renou, B., Vandel, A., Gicquel, L., and Cabot, G. 2014. Flame propagation in aeronautical swirled multi-burners: Experimental and numerical investigation. *Combust. Flame*, **161**, 2387–2405.

Birch, A., Brown, D., and Dodsen, M. 1981. Ignition probabilities in turbulent mixing flows. *Proc. Combust. Inst.*, **18**, 1755–80.

Boileau, M., Staffelbach, G., Cuenot, B., Poinsot, T., and Berat, C. 2008. LES of an ignition sequence in a gas turbine engine. *Combust. Flame*, **154**, 2–22.

Bourgouin, J.F., Durox, D., Schuller, T., Beaunier, J., and Candel, S. 2013. Ignition dynamics of an annular combustor equipped with multiple swirling injectors. *Combust. Flame*, **160**, 1398–1413.

Bulat, G., Jones, W., and Marquis, A. 2013. Large eddy simulation of an industrial gas-turbine combustion chamber using the sub-grid pdf method. *Proc. Combust. Inst.*, **34**, 3155–3164.

Cavaliere, D. 2013. Blow-off in gas turbine combustors. Ph.D. thesis. University of Cambridge, UK.

Cordier, M., Vandel, A., Cabot, G., Renou, B., and Boukhalfa, A. 2013. Laser-induced spark ignition of premixed confined swirled flames. *Combust. Sci. Technol.*, **185**:(3), 379–407.

Escalpez, L., Riber, E., and Cuenot, B. 2015. Ignition probability of a partially premixed burner using LES. *Proc. Combust. Inst.*, **35**, 3133–3141.

Eyssartier, A., Cuenot, B., Gicquel, L., and Poinsot, T. 2013. Using LES to predict ignition sequences and ignition probability of turbulent two-phase flames. *Combust. Flame*, **160**, 1191–1207.

Jones, W., Marquis, A., and Prasad, V. 2012. LES of a turbulent premixed swirl burner using the eulerian stochastic field method. *Combust. Flame*, **159**, 3079–3095.

Jones, W., and Prasad, V. 2011. LES-PDF simulation of a spark ignited turbulent methane jet. *Proc. Combust. Inst.*, **33**, 1355–1363.

Lacaze, G., Richardson, E., and Poinsot, T. 2009. Large eddy simulation of spark ignition in a turbulent methane jet. *Combust. Flame*, **156**, 1993–2009.

Lefebvre, A. 1999. *Gas Turbine Combustion*, 2nd ed, Taylor and Francis, London.

Lewis, B., and Elbe, G. 1987. *Combustion, Flames and Explosions of Gases*, Harcourt Brace Jovanovich, London.

Machover, E., and Mastorakos, E. 2015. Spark ignition of annular non-premixed combustors. *Exp. Therm. Fluid Sci.*, **73**, 64–70.

Machover, E. and Mastorakos, E. 2017. Experimental investigation on spark ignition of annular premixed combustors. *Combust. Flame*, **178**, 148–157.

Mastorakos, E. 2009. Ignition of turbulent non-premixed flames. *Prog. Energy Combust. Sci.*, **35**, 57–97.

Neophytou, A., Richardson, E., and Mastorakos, E. 2012. Spark ignition of turbulent recirculating non-premixed gas and spray flames: A model for predicting ignition probability. *Combust. Flame*, **159**, 1503–1522.

Philip, M., Boileau, M., Vicquelin, R., Riber, E., Schmitt, T., Cuenot, B., Durox, D., and Candel, S. 2015a. Large eddy simulations of an annular multiple-injector combustor. *Proc. Combust. Inst.*, **35**, 3159–3166.

Philip, M., Boileau, M., Vicquelin, R., Schmitt, T., Durox, D., Bourgouin, J., and Candel, S. 2014. Ignition sequence in a multi-injector combustor. *Phys. Fluids*, 26.

Philip, M., Boileau, M., Vicquelin, R., Schmitt, T., Durox, D., Bourgouin, J., and Candel, S. 2015b. Ignition sequence in a multi-injector combustor. *J. Eng. Gas Turbines Power*, **137**, 3.

Pope, S. 2000. *Turbulent Flows*, Cambridge University Press, London.

Richardson, E.S., and Mastorakos, E. 2007. Numerical investigation of forced ignition in laminar counterflow non-premixed methane-air flames. *Combust. Sci. Technol.*, **179**, 21–37.

Sitte, M., Bach, E., Kariuki, J., Bauer, H.J., and Mastorakos, E. 2016. Simulations and experiments on the ignition probability in turbulent premixed bluff-body flames. *Combust. Theor. Model.*, **20**, 548–565.

Soworka, T., Gerendas, M., and Eggels, R. 2013. Numerical investigation on ignition preceated at a lean burn combustor at sub-atmospheric conditions. Presented at the ASME Turbo Expo, June 16–20, Düsseldorf, Germany.

Subramanian, V., Domingo, P., and Vervisch, L. 2010. Large eddy simulation of forced ignition of an annular bluff-body burner. *Combust. Flame*, **157**, 579–601.

Triantafyllidis, A., Mastorakos, E., and Eggels, R. 2009. Large eddy simulation of forced ignition of a non-premixed bluff-body methane flame with conditional moment closure. *Combust. Flame*, **156**, 2328–2345.

Turns, S. 2000. *An Introduction to Combustion: Concepts and Applications*, McGraw-Hill, London.

Vagelopoulos, C., and Egolfopoulos, F. 1998. Direct experimental determination of laminar flame speeds. *Symp. (Int.) Combust.*, **27**, 513–519.

Worth, N., and Dawson, J. 2013. Modal dynamics of self-excited azimuthal instabilities in an annular combustion chamber. *Combust. Flame*, **160**, 2476–2489.